Backscatter of turbulent kinetic energy in chemically-reacting compressible flows

By J. Urzay, J. O'Brien, M. Ihme, P. Moin AND A. Saghafian

1. Motivation and objective

This study addresses the dynamics of kinetic-energy backscatter in the context of large-eddy simulations (LES) of turbulent chemically-reacting compressible flows. As a case study, a-priori analyses of direct numerical simulations (DNS) of reacting and inert supersonic, time-developing, hydrogen-air turbulent mixing layers with complex chemistry and multi-component diffusion are conducted herein to examine the effects of compressibility and combustion on subgrid-scale (SGS) backscatter of kinetic energy. General formulations of SGS backscatter with dilatation are provided, including an LES-based energy-transfer diagram that illustrates the conversion dynamics. Lastly, influences of SGS backscatter on the Boussinesq eddy viscosity are analyzed.

2. Background

The energy-cascade hypothesis predicts that turbulent kinetic energy is generated at the largest scales in a flow and then transferred to progressively smaller and smaller scales until it is dissipated by molecular viscosity. This energy cascade typically holds in a statistically-averaged sense, but it does not always describe the local behavior of a turbulent flow. The turbulent dissipation associated with the smallest, viscous scales, is actually the difference between two energy fluxes, namely, the forwardscatter, corresponding to the classical energy cascade, and the backscatter, a reversal of this process in which energy is transferred from the small scales back to the large scales (Lesieur & Métais 1996).

The backscatter of energy can be understood by analyzing energy fluxes in wavenumber space or in physical space (see Figure 1). In spectral space, backscatter is associated with triadic interactions between large and small scales in a flow, and arises as a negative rate of energy change of an individual wavenumber mode (Brasseur & Wei 1994). In physical space, local backscatter of kinetic energy is often observed as negative values of the subgrid-scale (SGS) dissipation upon filtering velocity fields obtained from Direct Numerical Simulations (DNS) (Piomelli *et al.* 1991) or from experiments (Tao *et al.* 2002). In physical-space analyses of energy fluxes, the negative value of the SGS dissipation (which is denoted below as ϵ_{SGS}) is interpreted as the reverse flux of energy from small to large scales that is required to preserve the resolved turbulent motion once the momentum of the small eddies has been filtered out.

If modelization of the SGS turbulent-momentum transfer in LES is endeavored by using the Boussinesq eddy-viscosity hypothesis, the eddy-viscosity coefficient restricts the net dissipation dynamics. In low-speed flows the Boussinesq eddy viscosity becomes negative in regions where backscatter occurs. The SGS backscatter acts as a source term in the kinetic-energy equation; if it persists in low speed flows, kinetic energy will tend to accumulate in the supergrid by means of a reverse turbulent-diffusion process,
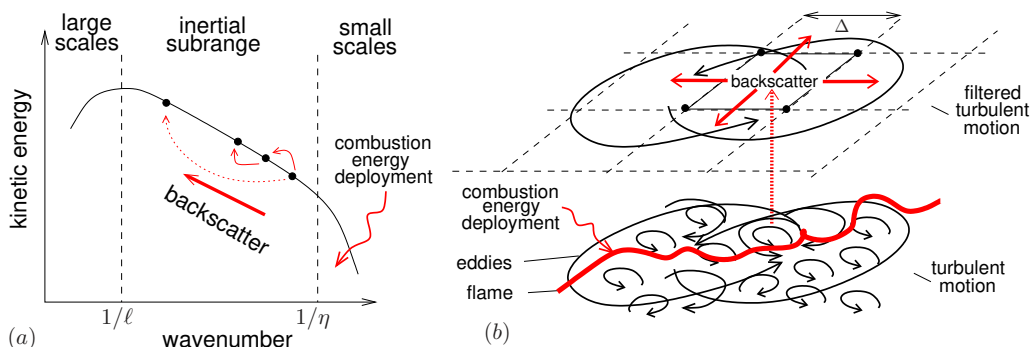
FIGURE 1. Sketch of backscatter processes through interaction of scales in (a) spectral and (b) physical spaces. Here ℓ, η, and Δ denote, respectively, the integral scale, Kolmogorov length, and filter width.

causing computations to become numerically unstable (Lund *et al.* 1993). Backscatter is commonly observed in DNS and experiments (for instance, as much as 40% of the flow volume may be undergoing backscatter in incompressible turbulent channel flows); yet in the mean, the classical direct energy cascade is observed (Piomelli *et al.* 1991). However, purely-dissipative SGS models based on the Boussinesq eddy-viscosity hypothesis, such as the Smagorinsky model, do not account for backscatter. The dynamic Smagorinsky model developed by Germano *et al.* (1991) in principle allows for backscatter by calculating the Smagorinsky constant dynamically as a function of space and time, which also results in some loss of information of the sign and magnitude of the local SGS dissipation, and, in practice, generally suppresses backscatter. Extensions of these models that account for local backscatter have been done by Ghosal *et al.* (1995) based on studying the kinetic-energy depletion in the subgrid.

Stochastic forcing with uncorrelated noise is also used to account for effects of SGS backscatter (Carati *et al.* 1995). However, backscatter is produced by turbulent eddies with non-zero decorrelation time, and therefore such descriptions are untenable. In addition, this study shows that SGS backscatter is intimately related to volumetric expansion in compressible flows, which may point to additional competition between acoustic and energy-deployment time scales.

Engineering applications in hypervelocity propulsion, such as supersonic combustion ramjets, typically operate high-speed chemically-reacting turbulent flows. These combined effects complicate the dynamics of turbulence and may lead to generation or destruction of turbulent kinetic energy due to to a number of phenomena involving shock waves, eddy shocklets, and conversion into thermal energy by pressure-dilatation effects (Lele 1994). In turbulent reacting flows, thermal energy is deposited at the smallest scales. In these scales, molecular diffusion dominates and fuel and oxidizer burn in flames releasing chemical heat. In fact, combustion represents an additional source of flow dilatation driven by thermal expansion or variable-density effects, which can deploy extra kinetic energy into the system through pressure-dilatation work and flows driven by flame-front instabilities (Luo 1999; Williams 1985).

The remainder of this report is organized as follows. The formulation, computational details, and main simulation results are outlined in Section 3. Analysis of the SGS backscatter dynamics, including effects on the eddy viscosity, is carried out in Section 4.
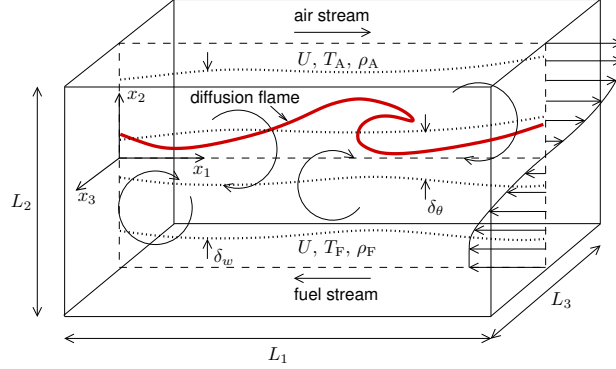
FIGURE 2. Sketch of the computational setup: A turbulent mixing layer develops between two supersonic streams of air and hydrogen diluted with nitrogen.

In Section 5 an energy-flux diagram is proposed. Finally, some brief conclusions are drawn in Section 6. Further details are provided in a recent publication (O'Brien *et al.* 2013).

3. The hydrogen-air supersonic turbulent mixing layer

The present study extends the understanding of backscatter phenomena to both compressible and reacting flows by performing an *a-priori* study of DNS results of a time-developing supersonic turbulent mixing layer. The computational setup involves two supersonic free streams of air and fuel flowing in opposite directions at the same velocity U, as depicted in Figure 2. The fuel stream is composed of 6.7% of gaseous hydrogen (H_2) by mass, balanced with gaseous nitrogen (N_2). The temperature of the air and fuel stream are $T_A = 1500$ K and $T_F = 500$ K, respectively, both at a static pressure $p_\infty = 2$ bar. The main parameters of the simulations are listed in Table 1 and described below.

3.1. *Formulation*

For obtaining the DNS results analyzed in this study, the Navier Stokes and species conservation equations

$$\frac{\partial \rho}{\partial t} + \frac{\partial \rho u_i}{\partial x_i} = 0, \tag{3.1}$$

$$\frac{\partial \rho u_i}{\partial t} + \frac{\partial}{\partial x_j}(\rho u_i u_j) = -\frac{\partial p}{\partial x_i} + \frac{\partial \tau_{ij}}{\partial x_j}, \tag{3.2}$$

$$\frac{\partial \rho Y_k}{\partial t} + \frac{\partial}{\partial x_i}(\rho u_i Y_k) = -\frac{\partial}{\partial x_i}(\rho V_{i,k} Y_k) + \dot{\omega}_k, \quad k = 1, \ldots N, \tag{3.3}$$

$$\frac{\partial \rho E}{\partial t} + \frac{\partial}{\partial x_i}(\rho u_i E) = -\frac{\partial p u_i}{\partial x_i} + \frac{\partial \tau_{ij} u_i}{\partial x_j} - \frac{\partial q_i}{\partial x_i}, \tag{3.4}$$

were integrated numerically together with the equation of state $p = \rho R^0 T/W$. In this formulation, u_i are the velocity components, p is the static pressure, T is the static temperature, ρ is the density, R^0 is the universal gas constant, W is the average molecular weight of the mixture, E is the total energy (including thermal, kinetic and chemical energy), and N is the number of species. Similarly, $\tau_{ij} = 2\mu(S_{ij} - \Delta_v \delta_{ij}/3)$ is the viscous stress tensor, with μ the molecular viscosity of the mixture, $S_{ij} = (1/2)(\partial u_i/\partial x_j + \partial u_j/\partial x_i)$ the strain-rate tensor, and $\Delta_v = S_{ii}$ the flow dilatation. The variables Y_k and

$\dot{\omega}_k$ denote the mass fraction and rate of production of species k, respectively. The diffusion velocities $V_{i,k}$ are calculated using the Curtiss-Hirschfelder approximation. The heat flux q_i is computed from the expression $q_i = -\lambda \partial T / \partial x_i + \sum_{k=1}^{N} \rho h_k Y_k V_{i,k}$, with λ the thermal conductivity and h_k the sensible enthalpy of species k. In these calculations, the Dufour effect and the thermodiffusion and barodiffusion mechanisms of heat and mass transport are neglected. The dynamic viscosity μ of the mixture depends on temperature and is obtained from Wilke's mixing rule based on the individual viscosities of the species, which are calculated from collision parameters. The specific heat capacities are computed from NASA polynomials. Lastly, the mass diffusivities are calculated by imposing constant Lewis numbers, whose values are given in Section 2.3. The H_2/O_2 mechanism by Hong *et al.* (2010), which consists of 20 steps and $N = 9$ species (e.g. H_2, O_2, H_2O, OH, HO_2, H_2O_2, O, H, and N_2) is used to describe the reaction chemistry. In the inert cases, the chemistry is inhibited by turning off all chemical sources in the species conservation equations (3.3).

3.2. *Computational setup*

Equations (3.1)-(3.4) were integrated numerically using a finite-volume scheme that minimizes dissipation error while still preserving stability (Khalighi *et al.* 2011). The numerical simulations are performed on a Cartesian grid of $768 \times 320 \times 192$ elements in the x_1, x_2, and x_3 directions, respectively, whose dimensions L_1, L_2, and L_3 are sufficiently large to accommodate the integral scales of the flow (see Table 1). Further details on the computational setup can be found in a recent publication (O'Brien *et al.* 2013), including initialization of the mixing layer, numerical resolution, and numerical verification against other simulations.

Reynolds and Favre filtering of any variable f are denoted by the operator $\overline{f}$ and $\widetilde{f}$, respectively. Here, the differential filter of Germano (1986) is used with a uniform filter width given by Δ. Similarly, the RANS averages are performed along the homogeneous directions x_1 and x_3, and the corresponding Reynolds and Favre operators are written as $\underline{f}$ and $\underset{\sim}{f}$, respectively. Lastly, the planar average of f over the homogeneous directions is denoted as $\langle f \rangle$, which coincides with the RANS average $\underline{f}$ defined above, but it is kept here as a separate operator for avoiding confusion between RANS quantities and planar averages of filtered quantities.

An objective of this study is to assess the effect of combustion on the dynamics of backscatter in the supersonic mixing layer. For this purpose, a simple (and perhaps the simplest) approach is taken in which reacting and inert flows are compared under the criteria that a) they are in the selfsimilar regime as described below, b) the instantaneous momentum thicknesses are the same, which translates into the same instantaneous Reynolds number $\mathrm{Re}_\theta^\star = U\delta_\theta^\star/\nu_\mathrm{A}$, and c) the joint dimensionless parameters in Table 1 are the same at the beginning of the computations. Here ν_A is the kinematic viscosity on the air side. By using this procedure, some degree of dynamic similarity between the instantaneous solutions selected for the reacting and inert mixing layers is expected, in which the history of the initial conditions is lost once the selfsimilar period begins and the exact value of the time coordinate becomes irrelevant. The DNS data were analyzed at the momentum thickness Reynolds number $\mathrm{Re}_\theta^\star = 1044$ in both the inert and reacting cases, where $\delta_\theta^\star = 18.6\delta_\theta^0$ is the final momentum thickness. At this time instant, both flows are in the selfsimilar regime.

Parameter	Description	Value (inert)	Value (reacting)
Parameters at the end of the simulations:			
$\mathrm{Re}_\theta^\star$	Reynolds number (momentum-based)	1044	1044
$\mathrm{Re}_w^\star$	Reynolds number (vorticity-based)	6352	8746
$\mathrm{Re}_\lambda^\star$	Taylor Reynolds number	42	75
$\mathrm{Ma}_t^\star$	Turbulent Mach number	0.51	0.42
$\eta^\star$	Kolmogorov length (in units of grid spacing)	0.7	1.0
$L_1/\ell_1^\star$	Streamwise domain size (in units of integral length)	18.4	15.1
$L_3/\ell_3^\star$	Spanwise domain size (in units of integral length)	17.9	9.7
Joint parameters:			
Re_θ^0	Initial Reynolds number (momentum-based)	56	
Re_w^0	Initial Reynolds number (vorticity-based)	224	
Ma_C	Convective Mach number	2.47	
Ma_A	Air-side Mach number	2.25	
Ma_F	Fuel-side Mach number	2.73	
Z_{st}	Stoichiometric mixture fraction	0.31	
L_1/δ_θ^0	Streamwise domain size (in units of momentum thickness)	315	
L_2/δ_θ^0	Cross-shear domain size (in units of momentum thickness)	211	
L_3/δ_θ^0	Spanwise domain size (in units of momentum thickness)	79	
s	Fuel-air density ratio	1.56	
Pr	Prandtl number	0.72	
Le_{H_2}	Lewis number (H_2)	0.32	
Le_{O_2}	” (O_2)	1.15	
Le_{N_2}	” (N_2)	1.32	
Le_{H_2O}	” (H_2O)	0.86	
Le_{HO_2}	” (HO_2)	1.16	
$\mathrm{Le}_{H_2O_2}$	” (H_2O_2)	1.17	
Le_{OH}	” (OH)	0.76	
Le_{H}	” (H)	0.19	
Le_{O}	” (O)	0.75	

TABLE 1. Values of the main dimensionless parameters used in the simulations.

3.3. *Selfsimilar region*

After a transient in which the influences of the initial conditions are noticeable, a quasi-linear regime is observed in the growth of the momentum thickness δ_θ, the vorticity
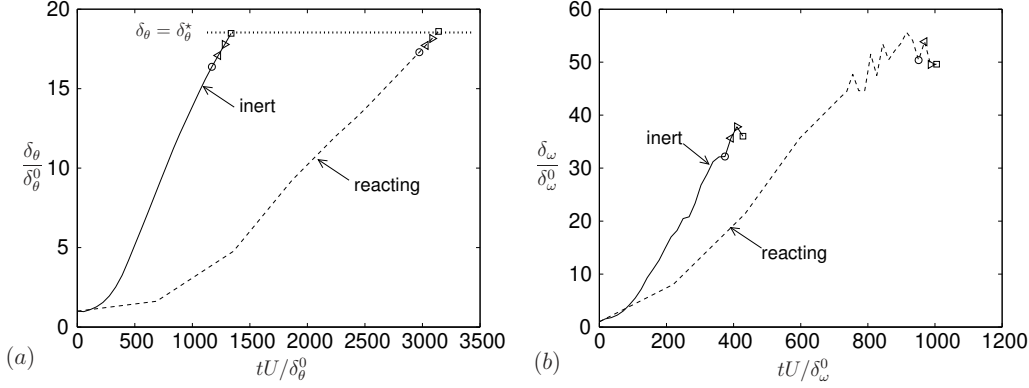
FIGURE 3. Time variations of (a) momentum thickness and (b) vorticity thickness for inert (solid lines) and reacting (dashed lines) simulations. The time instants denoted by the symbols $\circ, \triangleright, \triangleleft$, and $\square$, are spaced $U\Delta t/\delta_\theta^0 = 71.2$ time units (e.g. 2.84 times the strain time $\delta_\theta^\star/U$). Quantities denoted by the symbol $\square$ correspond to the final momentum thickness $\delta_\theta = \delta_\theta^\star$.

thickness δ_w and, for the reacting cases, in the mean chemical-production rate of water vapor per unit of in-plane surface $\underline{\dot{\mathcal{W}}}_{H_2O}$, as shown in Figure 3 and Figure 5. Here, δ_θ and δ_w are computed from the definitions $\delta_\theta = \int_{-\infty}^{\infty}(\rho/\rho_A)[1-(\underline{u}_1/U)^2]dx_2/[2(1+s)]$, and $\delta_w = \int_{-\infty}^{+\infty}|\underline{\omega}_3|dx_2/|\underline{\omega}_{3,\mathrm{max}}|$, with $\underline{\omega}_3 = \partial\underline{u}_1/\partial x_2$ the mean spanwise vorticity. For the reacting cases, the mean chemical-production rate of water vapor is calculated as $\underline{\dot{\mathcal{W}}}_{H_2O} = \int_{-\infty}^{+\infty}\underline{\dot{w}}_{H_2O}dx_2$, where $\underline{\dot{w}}_{H_2O}$ is the production rate of water-vapor mass per unit volume. The period of quasi-linear growth of δ_θ and $\underline{\dot{\mathcal{W}}}_{H_2O}$ is defined here as the period of selfsimilar evolution, during which the turbulence characteristics are approximately selfsimilar when non-dimensionalized with the instantaneous large spatial scale δ_θ and the long time scale δ_θ/U. The choice of δ_θ as spatial scale is convenient here because it is an integral quantity that varies smoothly and takes explicitly into account the density variations in the mixing layer.

The vorticity and momentum mixing-layer thicknesses grow in time as a result of the momentum transfer between the free streams and the corresponding vorticity generation. In the first approximation, the relation $(1/U)d\delta_\theta/dt = C_\theta$ represents the growth of the momentum thickness in the selfsimilar region, with C_θ a dimensionless constant that depends in a complex manner on the aerothermochemical parameters of the problem. In particular, these DNS results show that $C_\theta = 7.6 \cdot 10^{-3}$ and $C_\theta = 1.4 \cdot 10^{-2}$ for the reacting and inert mixing layers, respectively. At the end of the simulations, the ratio δ_w/δ_θ is 6.1 and 8.3 for the inert and reacting cases, respectively. Specifically, Figure 3 shows that δ_θ and δ_w grow more slowly for the reacting simulations. Furthermore, it is observed in Figure 3(a) that the momentum thickness at the end of the simulations, $\delta_\theta = \delta_\theta^\star$, lies within the quasi-linear growth zone that is representative of the selfsimilar period in both inert and reacting cases.

The selfsimilarity of the mixing layer is also revealed by the collapse of the profiles of mean streamwise velocity $\underline{u}_1$ and streamwise Reynolds stress $\underline{\rho u_1'' u_1''}$, as shown in Figure 4. These overall trends in first and second-order statistics are also in agreement with earlier studies in similar configurations with simpler transport and kinetic descriptions.
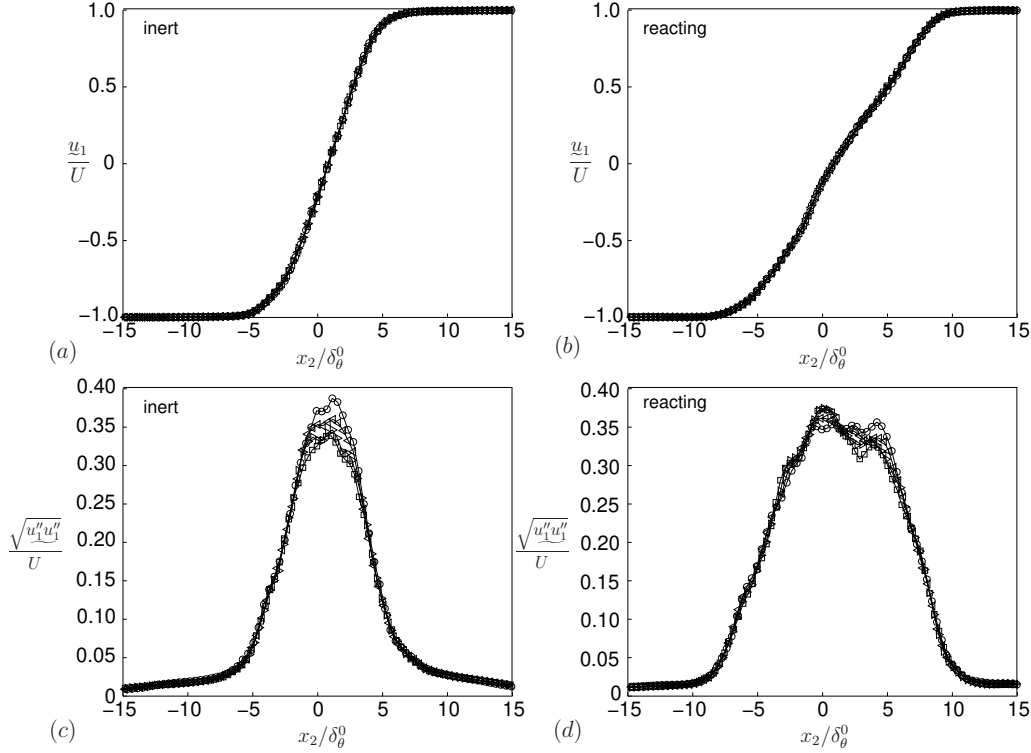
FIGURE 4. (a,b) Collapse of the mean streamwise velocity and (c,d) streamwise Reynolds stress for inert and reacting mixing layers. Refer to caption in Figure 3 for the symbols ∘,▷, ◁, and □.

4. Dynamics of SGS backscatter of kinetic energy with dilatation effects

The aerothermochemical variables are normalized here with the instantaneous momentum thickness $\delta_\theta^\star$ as the unit of spatial scale, the characteristic strain time $\delta_\theta^\star/U$ as the unit of time, ρ_A as the unit of density, U as the unit of velocity, $\rho_A U^2$ as the unit of pressure, and μ_A the unit of dynamic viscosity. In these variables, the filtered version of the momentum equation (3.2) becomes

$$\frac{\partial}{\partial t}(\overline{\rho}\widetilde{u}_i) + \frac{\partial}{\partial x_j}(\overline{\rho}\widetilde{u}_i\widetilde{u}_j) = -\frac{\partial \overline{p}}{\partial x_i} + \frac{1}{\mathrm{Re}_\theta^\star}\frac{\partial \overline{\tau}_{ij}}{\partial x_j} - \frac{\partial \mathcal{T}_{ij}}{\partial x_j}, \tag{4.1}$$

where the tensor $\mathcal{T}_{ij} = \overline{\rho}\widetilde{u_i u_j} - \overline{\rho}\widetilde{u}_i\widetilde{u}_j$ describes the dimensionless residual stresses.

A conservation equation for the large-scale kinetic energy, $k = \widetilde{u}_i\widetilde{u}_i/2$, can be obtained by multiplying (4.1) by $\widetilde{u}_i$ and using Eq. (3.1), which gives

$$\frac{\partial \overline{\rho}k}{\partial t} + \frac{\partial}{\partial x_i}(\overline{\rho}\widetilde{u}_i k) = \alpha + \Pi - \epsilon_v - \epsilon_{\mathrm{SGS}}, \tag{4.2}$$

with α a transport term that just redistributes kinetic energy. Conversely, the last three terms on the right-hand side of Eq. (4.2) are sources and sinks of large-scale kinetic energy. More importantly, Π represents a dimensionless pressure-dilatation work done by the large scales, and which is given by
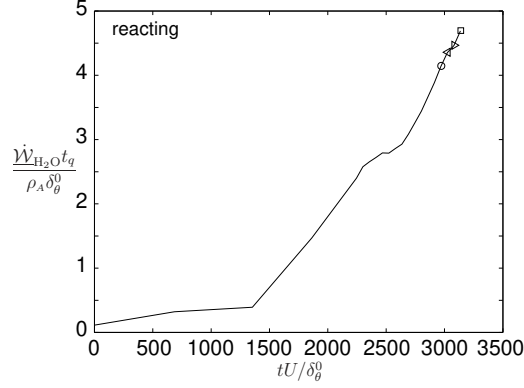
$$\Pi = \overline{p}\widetilde{\Delta}_v, \tag{4.3}$$

FIGURE 5. Mean rate of water-vapor mass production per unit of in-plane surface $\underline{\dot{\mathcal{W}}}_{H_2O}$ as a function of time in the reacting mixing layer. Refer to caption in Figure 3 for the symbols ∘,▷, ◁, and □. The characteristic chemical time t_q is estimated from the low pressure-limit of the rate constant of the recombination step $H + O_2 + N_2 \rightarrow HO_2 + N_2$ at the air-stream temperature T_A.

with $\widetilde{\Delta}_v = \partial \widetilde{u}_i / \partial x_i$ being the dilatation of the Favre-filtered velocity field. The pressure-dilatation work Π depends explicitly only on resolved quantities. Similarly, ϵ_v represents the dimensionless viscous dissipation

$$\epsilon_v = \frac{\overline{\tau}_{ij}\widetilde{S}_{ij}}{\mathrm{Re}_\theta^\star} = \frac{\overline{[2\mu(S_{ij} - \Delta_v \delta_{ij}/3)]}\widetilde{S}_{ij}}{\mathrm{Re}_\theta^\star}, \tag{4.4}$$

which is a sink of large-scale kinetic energy. In this formulation, $\widetilde{S}_{ij} = \partial \widetilde{u}_i / \partial x_j + \partial \widetilde{u}_j / \partial x_i$ is the strain rate of the Favre-filtered velocity field. Lastly, ϵ_{SGS} is the nondimensional SGS dissipation

$$\epsilon_{\mathrm{SGS}} = -\mathcal{T}_{ij}\widetilde{S}_{ij}, \tag{4.5}$$

which represents the rate at which kinetic energy is transferred from the resolved motion to the subgrid and vice-versa. The SGS dissipation ϵ_{SGS} is not a molecular dissipation, in that the energy transfer that it represents is due entirely to inertial processes at the filter level. In fact, at high Reynolds numbers, and for cutoff filters, the SGS dissipation is larger than the molecular dissipation ϵ_v by a factor of order $(\Delta/\eta)^{4/3}$, where η is the Kolmgorov length and Δ is somewhere in the inertial subrange, and represents the only considerale source of dissipative dynamics in Eq. (4.2). In addition, contrary to the viscous dissipation ϵ_v, the SGS dissipation ϵ_{SGS} may be locally positive, which indicates dissipation of large-scale kinetic energy or forwardscatter to the subgrid, or negative, which corresponds to the transfer of kinetic energy from the subgrid scales to the filtered velocity field, even though it is expected to forwardscatter energy in the spatially-averaged sense in accord with the classic energy-cascade theory. The case $\epsilon_{\mathrm{SGS}} < 0$, or energy transfer from the subgrid to the supergrid, is referred to as SGS backscatter of kinetic energy (Piomelli *et al.* 1991). The physical phenomenon represented by $\epsilon_{\mathrm{SGS}} < 0$ bears a strong resemblance with the reverse energy-transfer process described by the backscatter flux term that appears in the kinetic-energy equation in wavenumber space, although spectral backscatter and SGS backscatter are not strictly equivalent in inhomogeneous flows or when the spectral cutoff filter is not employed.

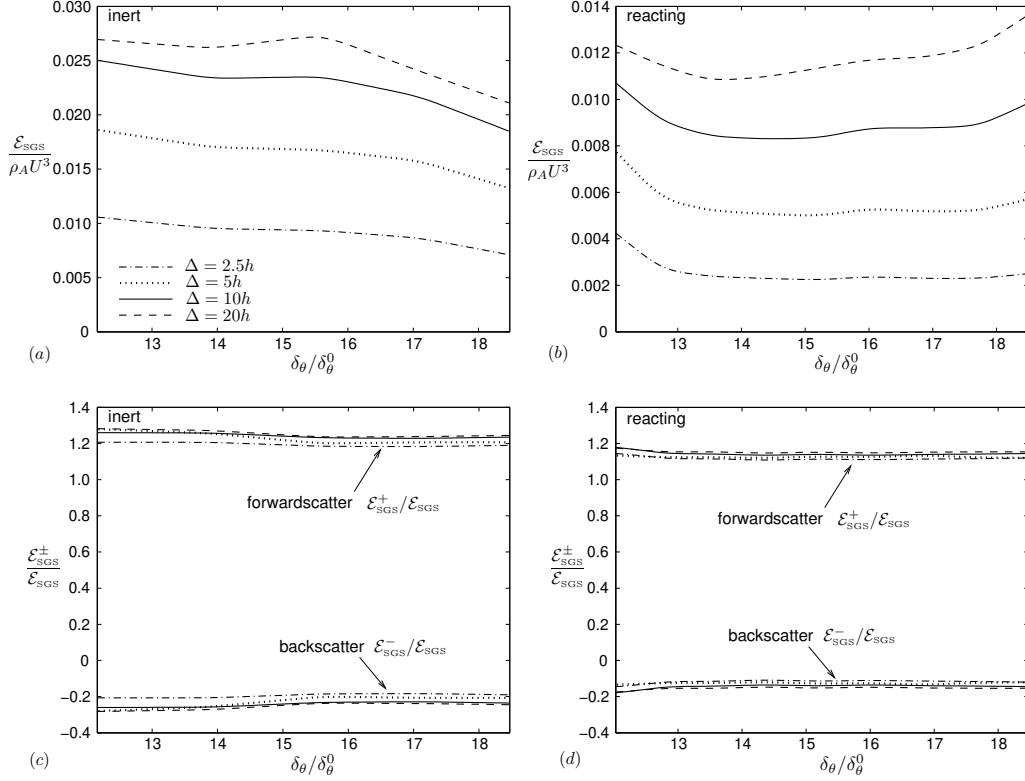In order to isolate positive and negative local contributions to the SGS dissipation and

FIGURE 6. (a,b) Temporal evolution of the integrated SGS dissipation $\mathcal{E}_{\text{SGS}}$ for different filter widths Δ (refer to legend in (a)). (c,d) Ratio of integrated SGS backscatter $\mathcal{E}_{\text{SGS}}^{-}$ and SGS forwardscatter $\mathcal{E}_{\text{SGS}}^{+}$ to the net $\mathcal{E}_{\text{SGS}}$.

pressure-dilatation work prior to planar averaging, the definitions $\epsilon_{\text{SGS}}^{+} = (1/2)(\epsilon_{\text{SGS}} + |\epsilon_{\text{SGS}}|) \geq 0$ for forwardscatter, and $\epsilon_{\text{SGS}}^{-} = (1/2)(\epsilon_{\text{SGS}} - |\epsilon_{\text{SGS}}|) \leq 0$ for backscatter, are used here in analogy to Piomelli *et al.* (1991), although a reverse sign is employed here to denote the more intuitive positive values of ϵ_{SGS} as forward-dissipating dynamics. Specifically, if ϵ_{SGS} becomes negative as in backscattering regions, then $\epsilon_{\text{SGS}}^{+}$ becomes zero, and vice versa. Additionally, the integral of the planar-averaged SGS dissipation in the cross-shear direction

$$\mathcal{E}_{\text{SGS}} = \int_{-\infty}^{+\infty} \langle \epsilon_{\text{SGS}} \rangle dx_2 \tag{4.6}$$

is utilized to monitor the temporal evolution of the net dissipation, forwardscatter and backscatter as the mixing layer grows. Similar to the expressions for $\epsilon_{\text{SGS}}^{+}$ and $\epsilon_{\text{SGS}}^{-}$, the SGS dissipation $\mathcal{E}_{\text{SGS}}$ can be decomposed into positive $\mathcal{E}_{\text{SGS}}^{+} > 0$ and negative $\mathcal{E}_{\text{SGS}}^{-} < 0$ contributions, which here refer to forwardscatter and backscatter, respectively. A similar decomposition into positive and negative pressure-dilatation work fluxes $\Pi^{+} = (1/2)(\Pi + |\Pi|)$ and $\Pi^{-} = (1/2)(\Pi - |\Pi|)$, can be used to describe the production of large-scale kinetic energy by flow expansion, $\Pi^{+} > 0$, and its destruction by flow compression, $\Pi^{-} < 0$.
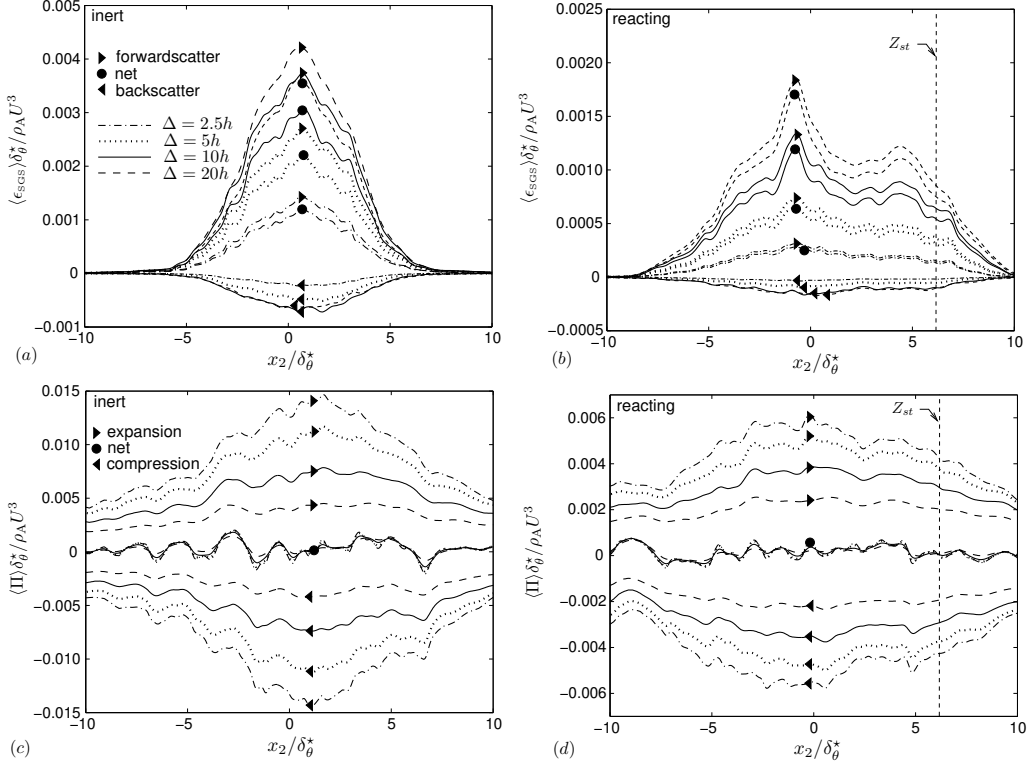
FIGURE 7. (a,b) Spatial distributions of the planar averaged dissipation, including backscatter $\langle \epsilon_{\rm SGS}^- \rangle$ (▶), forwardscatter $\langle \epsilon_{\rm SGS}^+ \rangle$ (◀) and net dissipation $\langle \epsilon_{\rm SGS} \rangle$ (●) for different filter widths Δ (refer to legend in (a)). (c,d) Spatial distributions of the planar-averaged large-scale pressure-dilatation work, including the expansion $\langle \Pi^+ \rangle$ (▶ symbol) and compression $\langle \Pi^- \rangle$ (◀ symbol) contributions, and the net value $\langle \Pi \rangle$ (● symbol).

4.1. *Spatio-temporal statistics*

The time evolution of $\mathcal{E}_{\rm SGS}$ for inert and reacting mixing layers is shown in Figure 6(a,b), in which the momentum mixing-layer thickness δ_θ has been used on the horizontal axis of the plot instead of the time coordinate t, since the mapping between both variables is approximately linear in the selfsimilar region. The integrated SGS dissipation $\mathcal{E}_{\rm SGS}$ does not undergo strong variations with time, which suggests that the characteristic value of $\langle \epsilon_{\rm SGS} \rangle$ decreases approximately with time as $\rho_{\rm A} U^3/\delta_\theta \propto 1/t$, as indicated by the order-of-magnitude estimate $\mathcal{E}_{\rm SGS} = O(\langle \epsilon_{\rm SGS} \rangle \delta_\theta)$ in Eq. (4.6). Figure 6(c,d) shows that at the final momentum thickness the integrated SGS backscatter $\mathcal{E}_{\rm SGS}^-$ amounts to approximately 23% and 18% of the net value in the inert and reacting mixing layers, respectively, thereby indicating a slightly lower relative intensity of backscatter for the reacting case. During the selfsimilar period, these conclusions are mostly insensitive to the value of the momentum thickness, and to the choice of the filter width.

Figure 7(a,b) reveals that backscatter occurs locally within the mixing layer due to the non-zero contribution of $\epsilon_{\rm SGS}^-$ to the net SGS dissipation, even though the overall planar-averaged energy transfer $\langle \epsilon_{\rm SGS} \rangle$ appears to occur from the large scales to the subgrid scales in accord with the traditional turbulent cascade. In addition, the levels of SGS dissipation increase with filter width, but the percentual increment in the SGS
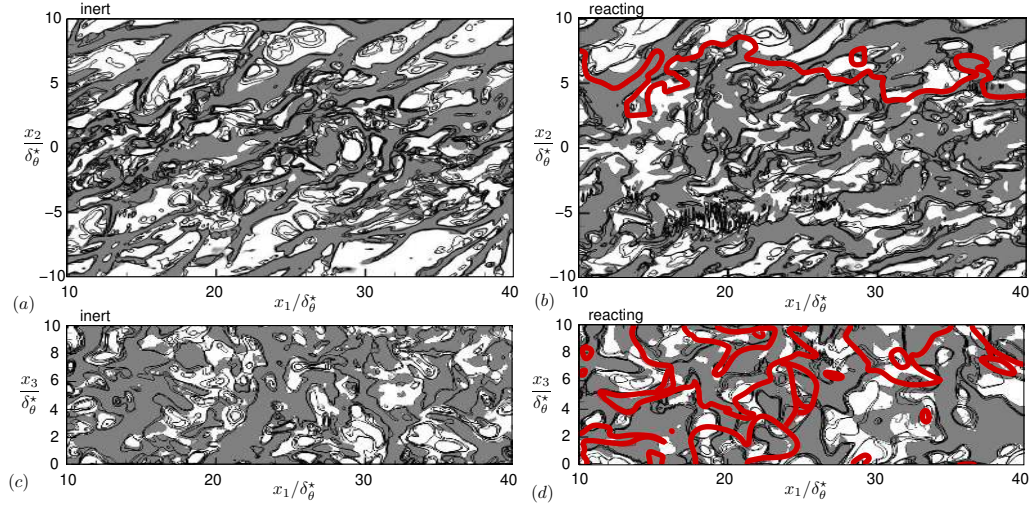
FIGURE 8. Isosurfaces of SGS backscatter $\epsilon_{\text{SGS}} < 0$ (white regions) and isocontours of positive pressure-dilatation work Π (solid lines) for $\Delta = 10h$, along with the stoichiometric line $Z_H = Z_{st}$ (thick red line, reacting case, color online) for (a,b) streamwise and (c,d) spanwise cross sections.

dissipation becomes smaller as the filter width increases, in qualitative agreement with the constancy predicted by the Kolmogorov's universal equilibrium theory for the turbulent dissipation across the inertial subrange.

The local values of the large-scale pressure-dilatation work are comparable to the SGS dissipation, as observed in Figure 7(c-d). Specifically, the planar average of the net large-scale pressure-dilatation work $\langle \Pi \rangle$ is found to be the result of the difference between two large fluxes of expansion $\langle \Pi^+ \rangle$ and compression $\langle \Pi^- \rangle$, which attain their maximum values near the centerline of the mixing layer where stagnation conditions. That these fluxes tend to cancel each other indicate some level of homogenization of the intense compression and expansion phenomena upon spatial averaging in the mixing layer. This effect is related to the fact that, despite the high speeds in this mixing layer, it is extremely difficult for the compressibility forced by the opposing supersonic streams to penetrate in the microscales and generate a coherent effect in the large scales unless much larger turbulent Mach numbers were to be achieved.

A central result of this investigation is that a correlation between backscatter and flow expansion exists as first observed in Figure 8, in which isocountours of $\epsilon_{\text{SGS}} < 0$ tend to visually follow closely those of $\Pi > 0$, this conclusion being mostly independent of the presence of chemical reactions in the mixing layer. In fact, no visible correlation in Figure 8(b,d) can be simultaneously detected between pressure-dilatation work and the stoichiometric line (which in the reacting cases is approximately indicative of the maximum flame temperature). A more detailed inspection of the same phenomena is made in Figure 9 over a larger computational domain by calculating the joint probability-density function (PDF) between ϵ_{SGS} and Π, which results in correlation coefficients -0.69 and -0.48 for the inert and reacting flows, respectively, in the region of the joint PDF shown in the insets.

In Figure 10(a-d), the joint PDFs of pressure dilatation work and SGS backscatter versus filtered H-element mixture fraction $\widetilde{Z}_H$ confirm that the chemical heat released
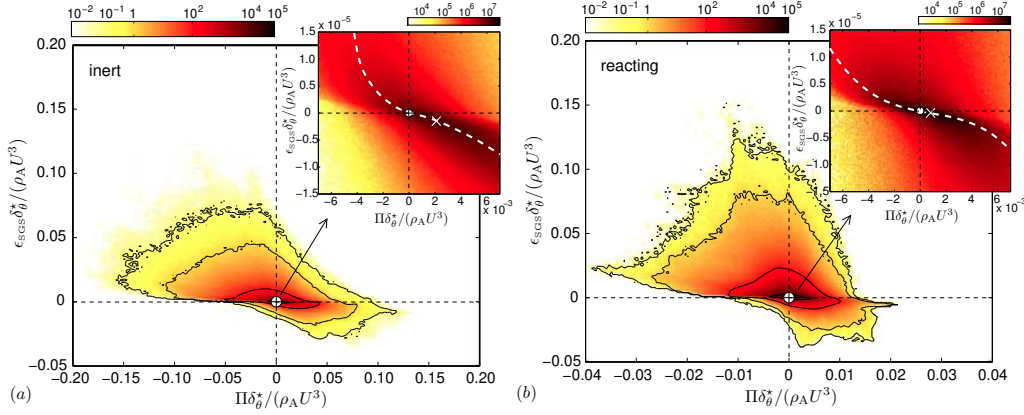
FIGURE 9. Isocontours of the joint PDF between SGS dissipation ϵ_{SGS} and pressure-dilatation work Π for $\Delta = 10h$, sampled in the volume $\{0.8 \leq x_1/\delta_\theta^\star \leq 16.0; \ 0.2 \leq x_2/\delta_\theta^\star \leq 4.0; \ -10.0 \leq x_3/\delta_\theta^\star \leq 10.0\}$. A magnification of the central zone of the joint PDFs is shown in the insets, which include the ridge of maximum probability (white dashed line) along with the point of global maximum probability (white $\times$).
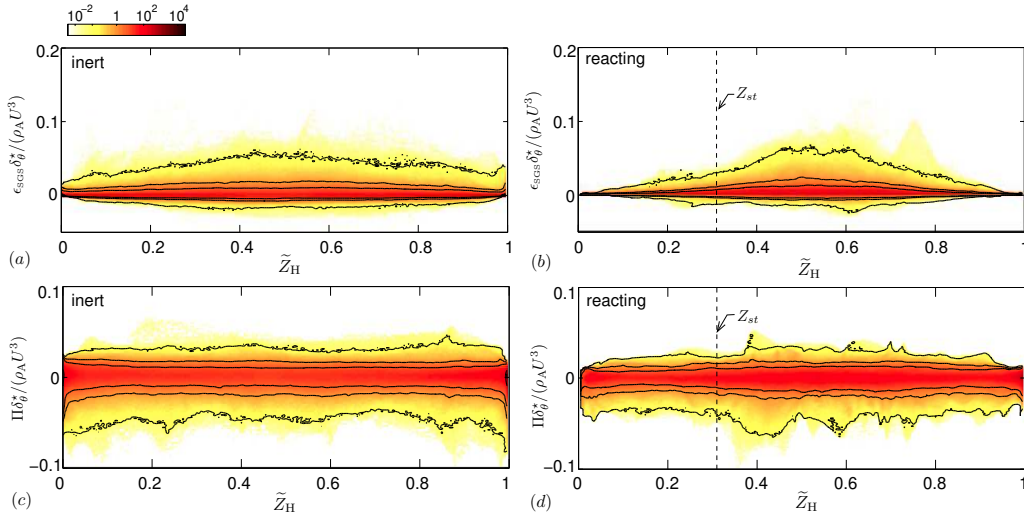

FIGURE 10. Isocontours of the joint PDF between the filtered mixture fraction $\widetilde{Z}_{\text{H}}$ and (a,b) SGS dissipation ϵ_{SGS} and (c,d) large-scale pressure-dilatation work Π for $\Delta = 10h$. Refer to caption in Figure 9 for the volume sampled to obtain the statistics.

by combustion has a very modest effect on these two quantities, in that no significant variations of Π and ϵ_{SGS} are observed with respect to $\widetilde{Z}_{\text{H}}$ as would typically be expected near stoichiometric conditions in reacting mixing layers, where the temperature reaches the maximum values. However, this conclusion should be taken with caution, as it may pertain only to diluted high-speed turbulent reacting flows dominated by compressibility effects.

The small effects of combustion on the backscatter dynamics in this mixing layer can be understood by consideration of the following. Two different sources of flow dilatation Δ_v are present in this flow. The first component of the dilatation is of order
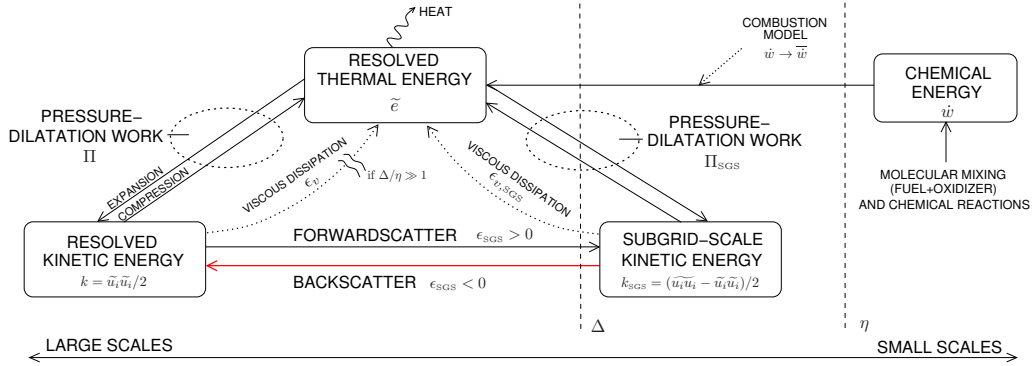
FIGURE 11. LES-based energy-transfer diagram including backscatter flux.

$\Delta_v \sim \gamma_A \mathrm{Ma}_A^2 U/\delta_\theta$ and pertains to the compressible nature of this high-speed mixing layer, causing characteristic large-scale variations in the mean density of order $\Delta\rho/\rho = \mathcal{O}(\rho_A U^2/p_\infty)$. The corresponding mechanism of energy transfer enhanced by this first component of Δ_v tends to peak in the large scales as a result of the cancellation of compression and expansion waves, as observed in Figure 7(c-d). The second component of the dilatation is of order $\Delta_v \sim UQY_F/[c_{p,A}T_A\delta_\theta(1+\mathcal{S})]$ and is related to the density fluctuations introduced by combustion, which produce characteristic large-scale variations in the mean temperature $\Delta T/T = \mathcal{O}(QY_F/(c_{p,A}T_A(1+\mathcal{S})))$, where Q is the overall heat of combustion per unit mass of fuel. The ratio of compressibility and combustion contributions to the dilatation represents an Eckert number $\mathrm{Ec} = \gamma_A \mathrm{Ma}_A^2 c_{p,A}T_A(1+\mathcal{S})/(QY_F)$, which becomes of order 10 for the present simulations. This indicates that the contribution of the high-speed flow compressibility to the pressure-dilatation overwhelms any addition that may be expected from the thermal expansion induced by combustion in this supersonic mixing layer.

4.2. *LES-based energy-transfer diagram*

Figure 11 illustrates the transfer of energy analyzed above in the context of LES formulations. In chemically-reacting compressible flows, the filtered version of the chemical heat released at the microscales, $\overline{\dot{w}}$, is transferred into filtered thermal energy $\widetilde{e}$, which leads to resolved temperature and density variations. In dilatational flows, part of the filtered pressure-dilatation work, namely $\Pi = \overline{p}\widetilde{\Delta}_v$, is responsible for the transfer of filtered thermal energy into resolved kinetic energy k and vice-versa. Part of the resolved kinetic energy forwardscatters into SGS kinetic energy, $k_{SGS} = (\widetilde{u_i u_i} - \widetilde{u}_i\widetilde{u}_i)/2$, a mechanism that prevails over viscous dissipation for sufficiently large filter widths. The kinetic energy in the subgrid can be dissipated through molecular diffusion generating thermal energy which, eventually, is irreversibly lost into heat. However, a fraction of k_{SGS} can also backscatter into resolved kinetic energy in accord with the transport equation

$$\frac{\partial \overline{\rho}k_{SGS}}{\partial t} + \frac{\partial}{\partial x_i}(\overline{\rho}\widetilde{u}_i k_{SGS}) = \alpha_{SGS} + \Pi_{SGS} + \epsilon_{SGS} - \epsilon_{v,SGS}, \tag{4.7}$$

where α_{SGS} is a redistribution term, and $\epsilon_{v,SGS}$ is a molecular dissipation, and $\Pi_{SGS} = \overline{p\Delta_v} - \Pi$ is the portion of the pressure-dilatation work diverted to the subgrid. An approximate equilibrium of k_{SGS} in the subgrid would suggest a balance between SGS pressure-dilatation and backscatter. In these simulations, however, only slightly more than half of the computational cells undergoing volumetric expansion have positive values of Π_{SGS}.
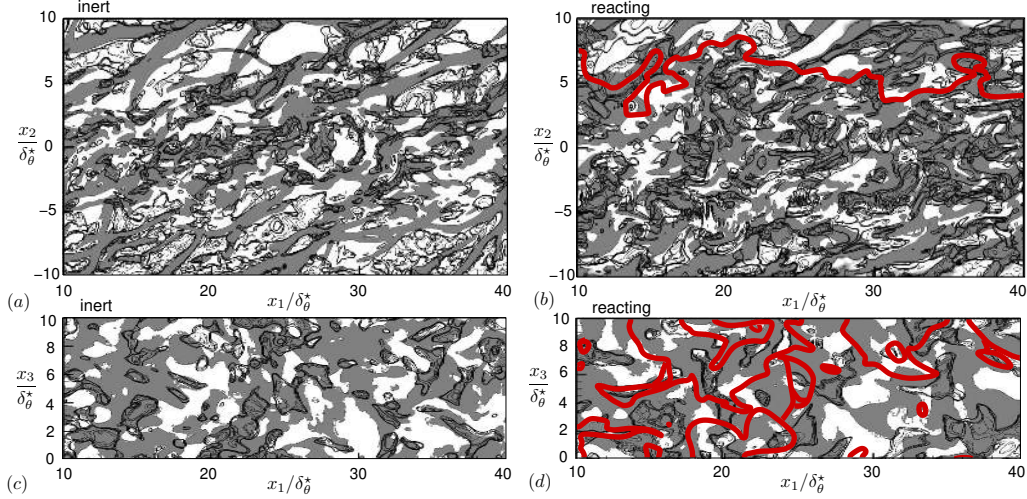
FIGURE 12. Isosurfaces of SGS backscatter $\epsilon_{\mathrm{SGS}} < 0$ (white regions), isocontours of negative eddy viscosity $\nu_t < 0$ (solid lines) for $\Delta = 10h$, along with the stoichiometric line $Z_{\mathrm{H}} = Z_{st}$ (thick red line, reacting case) for (a,b) streamwise and (c,d) spanwise cross sections.

Since backscatter occurs more often than $\Pi_{\mathrm{SGS}} > 0$ in regions subject to expansion, there are additional underlying physical phenomena needed to explain the correlation between Π and ϵ_{SGS}, which are deferred to future investigations.

4.3. *Boussinesq eddy viscosity under SGS backscatter and flow dilatation*

In the Boussinesq approximation, a perfect alignment between the SGS-stress and filtered strain-rate tensors is assumed, and the deviatoric part of the SGS stress tensor is modeled as

$$\mathcal{T}_{ij} - \frac{1}{3}\delta_{ij}\mathcal{T}_{kk} = -2\overline{\rho}\nu_t\left(\widetilde{S}_{ij} - \frac{\widetilde{\Delta}_v\delta_{ij}}{3}\right), \tag{4.8}$$

where δ_{ij} is the Kronecker tensor, and ν_t is a scalar eddy viscosity. Consider contracting expression (4.8) with $\widetilde{S}_{ij}$, and rearrange the resulting equation in the form

$$\nu_t = \frac{\epsilon_{\mathrm{SGS}}(1 + \Lambda)}{2\overline{\rho}\left(|\widetilde{S}|^2 - \dfrac{\widetilde{\Delta}_v^2}{3}\right)}, \tag{4.9}$$

where $\Lambda = \gamma_{\mathrm{A}}\mathrm{Ma}_{\mathrm{SGS}}^2\Pi/\epsilon_{\mathrm{SGS}}$ is represents the dimensionless ratio of the dilatation work done by the SGS dynamic pressure to the SGS dissipation, with Π and ϵ_{SGS} defined in Eqs. (4.3) and (4.5), respectively. In this formulation, the symbol $\mathrm{Ma}_{\mathrm{SGS}} = (2\overline{\rho}k_{\mathrm{SGS}}/3\gamma_{\mathrm{A}}\overline{p})^{1/2}$ is the SGS Mach number, which is a measure of the importance of compressibility effects in the subgrid scales.

In low-speed flows, the SGS Mach number is negligible for all filter widths and the resulting value of Λ is small in (4.9), thereby rendering the sign of the eddy viscosity fully correlated with the sign of the SGS dissipation, with $\nu_t < 0$ always occurring in the presence of SGS backscatter $\epsilon_{\mathrm{SGS}} < 0$ and vice versa (Piomelli *et al.* 1991).

In high-speed turbulent flows, an increasingly large amount of shocked regions of high $\mathrm{Ma}_{\mathrm{SGS}}$ numbers are transferred from the filtered field into the subgrid as Δ increases,
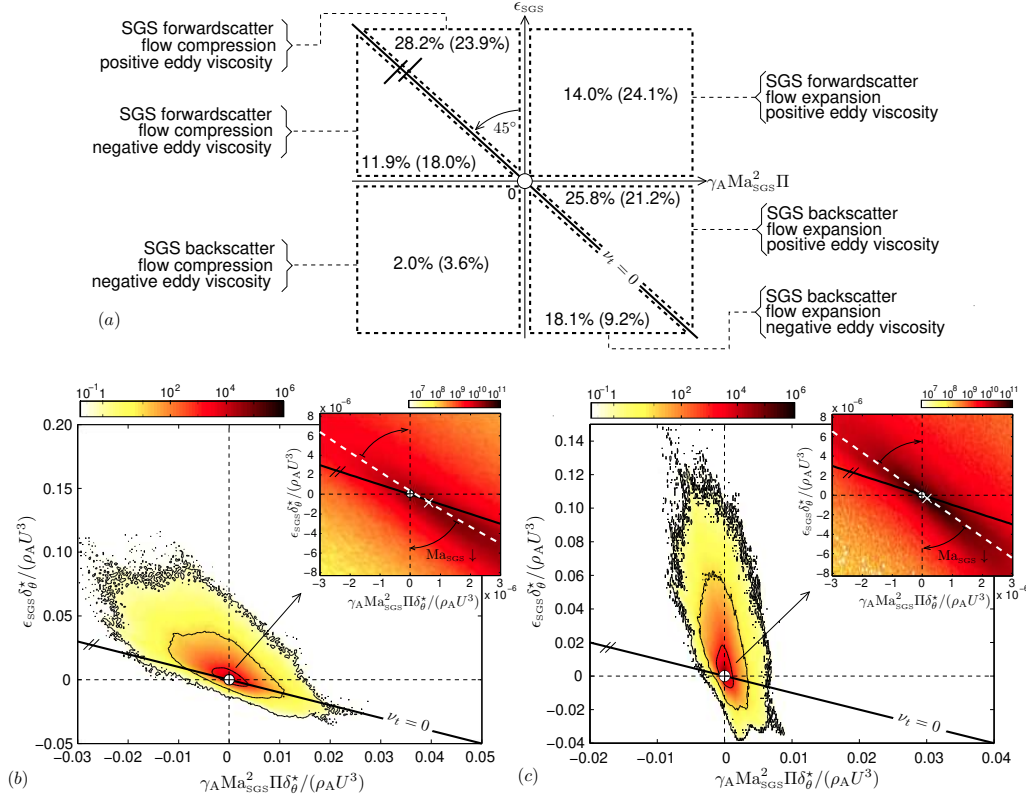
FIGURE 13. (a) Regime diagram representative of the different energy-conversion modes, quoting the corresponding volume fractions in inert and reacting (in between brackets) mixing layers. (b,c) Isocontours of the joint PDF between SGS dissipation ϵ_{SGS} and dilatation work by the SGS dynamic pressure $\gamma_A \mathrm{Ma}_{\mathrm{SGS}}^2 \Pi$ for $\Delta = 10h$. A magnification of the central zone of the joint PDFs is shown in the insets that includes the ridge of maximum probability (white dashed line) along with the point of global maximum probability (white ×). Refer to caption in Figure 9 for the volume sampled to obtain the statistics.

with $\mathrm{Ma}_{\mathrm{SGS}}$ increasing as a positive power of the filter width. In the present simulations the SGS Mach number attains relatively large local values even for small filter widths because of the intense expansion and compression waves in the mixing layer, which are rapidly transferred to the subgrid scales upon filtering the flow field.

In contrast to low-speed turbulent flows, negative values of the eddy viscosity in (4.8) are found to be not completely correlated with the occurrence of SGS backscatter in the high-speed flow analyzed in this study. This is shown by the isocontours in Figure 12, which also reveal that the sign of ν_t is mostly unrelated to combustion. These synergistic dynamics are summarized in Figure 13(a), which shows the budget of volume fractions undergoing each regime in terms of the possible combinations between the signs of ϵ_{SGS}, $\gamma_A \mathrm{Ma}_{\mathrm{SGS}}^2 \Pi$, and ν_t. In particular, the eddy viscosity is negative in approximately 32% (31%) of the sampled volume for $\Delta = 10h$, where brackets are utilized to indicate the percentages in the reacting case, the absence of brackets corresponding to the inert case. The 63% (41%) of this portion of the volume fraction with $\nu_t < 0$ is undergoing backscatter, with the remaining volume in a mode in which forwardscatter and compression occur

simultaneously. Equivalently, backscatter occurs in 46% (34%) of the volume, but the eddy viscosity is negative in only 43% (38%) of this portion. Increasing the filter width to $\Delta = 20h$ leads to a decrease in the volume fraction with $\nu_t < 0$ in backscatter mode, 38% (33%), and to an overall increase in the SGS Mach number.

Further insight is provided in Figure 13(b,c) by the joint PDFs of the SGS dissipation and the dilatation work done by the SGS dynamic pressure. For small values of the dilatation work done by the SGS dynamic pressure, which are the most probable in the mixing layer, a correlation is observed between ϵ_{SGS} and $\gamma_A \mathrm{Ma}_{\mathrm{SGS}}^2 \Pi$ as evidenced by the insets of Figure 13(b,c), by which backscatter tends to occurs in regions undergoing volumetric expansion with both positive and negative eddy viscosities. Specifically, the correlation coefficient in the region of the joint PDF shown in the insets of Figure 13(b,c) is -0.50 and -0.25 for the inert and reacting cases, respectively.

Since the SGS backscatter and the dilatation work of expansion done by the SGS dynamic pressure yield contributions of opposite sign in the eddy-viscosity Eq. (4.9), the correlation between these two quantities tends to moderate the effect of backscatter in generating negative amounts of eddy viscosity relative to purely incompressible flows. As shown above, the volume fraction undergoing backscatter with negative eddy viscosities decreases with filter width and SGS Mach number, a trend that is visualized in the insets of Figure 13(b,c) as a decrease in the angular shift between the line $\nu_t = 0$ and the high-probability ridge of the joint PDF of ϵ_{SGS} and $\gamma_A \mathrm{Ma}_{\mathrm{SGS}}^2 \Pi$. In the low-Mach number limit, the high probability ridge becomes a vertical line and the joint PDF has a negligible horizontal width, thereby indicating that $\nu_t < 0$ occurs exclusively in the presence of SGS backscatter and vice versa.

5. Conclusions

This investigation has shown that SGS backscatter occurs predominantly in flow regions undergoing expansion, which implies the existence of an underlying physical mechanism that involves dilatation and contributes to the reverse energy cascade. In addition, the high-speed compressibility effects induce a decorrelation between SGS backscatter and negative eddy viscosities, which increases for increasingly large values of the SGS Mach number and filter width, and which is not present in the low-speed regime. Furthermore, comparisons between reacting and inert mixing layers reveal that the combustion dynamics have a marginal impact on the backscatter and flow-dilatation distributions, at least in the diluted conditions studied in this work. Further investigations are warranted to isolate the conversion of combustion energy into turbulent fluid motion, and to study the influences of this reverse energy flux in SGS modeling.

REFERENCES

BRASSEUR, J. G. & WEI, C. S. 1994 Interscale dynamics and local isotropy in high Reynolds number turbulence within triadic interactions. *Phys. Fluids* **6**, 842–870.

CARATI, D., GHOSAL, S. & MOIN, P. 1995 On the representation of backscatter in dynamic localization models. *Phys. Fluids* **7**, 606–615.

GERMANO, M. 1986 Differential filters for the large-eddy numerical simulation of turbulent flows. *Phys. Fluids* **6**, 1755–1757.

GERMANO, M., PIOMELLI, U., MOIN, P. & CABOT, W. H. 1991 A dynamic subgrid-scale eddy viscosity model. *Phys. Fluids* **3**, 1760–1765.

GHOSAL, S., LUND, T. S., MOIN, P. & AKSELVOLL, K. 1995 A dynamic localization model for large-eddy simulation of turbulent flows. *J. Fluid Mech.* **286**, 229–255.

HONG, Z., DAVIDSON, D. & HANSON, R. 2010 An improved H_2/O_2 mechanism based on recent shock tube/laser absorption measurements. *Combustion and Flame* **158**, 633–644.

KHALIGHI, Y., NICHOLS, J. W., LELE, S., HAM, F. & MOIN, P. 2011 Unstructured large eddy simulations for prediction of noise issued from turbulent jets in various configurations. *AIAA* Paper no. 2011-2886.

LELE, S. 1994 Compressibility effects on turbulence. *Annu. Rev. Fluid Mech.* **26**, 211–254.

LESIEUR, M. & MÉTAIS, O. 1996 New trends in large-eddy simulations of turbulence. *Ann. Rev. Fluid Mech.* **28**, 45–82.

LUND, T. S., GHOSAL, S. & MOIN, P. 1993 Numerical experiments with highly variable eddy viscosity model. In *Engineering Applications of Large Eddy Simulations FED ASME* **162**, 7–11.

LUO, K. 1999 Combustion effects on turbulence in a partially premixed supersonic diffusion flame. *Combust. Flame* **119**, 417–435.

PANTANO, C. & SARKAR, S. 2002 A study of compressibility effects in the high-speed turbulent shear layer using direct simulation. *J. Fluid Mech.* **451**, 329–371.

PIOMELLI, U., CABOT, W., MOIN, P. & LEE, S. 1991 Subgrid-scale backscatter in turbulent and transitional flows. *Phys. Fluids A* **3**, 1766–1771.

TAO, B., KATZ, J. & MENEVEAU, C. 2002 Statistical geometry of subgrid-scale stresses determined from holographic particle image velocimetry measurements. *J. Fluid Mech.* **457**, 35–78.

O'BRIEN, J., URZAY, J., IHME, M., MOIN, P. & SAGHAFIAN A. 2013 Subgrid-scale backscatter of kinetic energy in reacting and inert supersonic hydrogen-air turbulent mixing layers. *J. Fluid Mech* (to appear).

WILLIAMS, F. A. 1985 *Combustion Theory.* Benjamin Cummings.